Robust Passive DoA Estimation for Low-SWaP Airborne Platforms: A Dual-Antenna Synthetic Aperture Approach

Leandro Geraldo da Costa, Rafael Cruz, Daniele Oliveira Silva, Romildo Henrique de Souza, and Felix Antreich
Instituto Tecnológico de Aeronáutica (ITA), São José dos Campos/SP – Brasil

***Abstract*— This work investigates a dual-antenna passive synthetic aperture Direction-of-Arrival (DoA) estimation technique for compact airborne sensors under simulated uncertainties in platform navigation and receiver synchronization. An electromagnetic environment incorporating spherical wave propagation and Doppler effects is implemented in an in-house radar simulator. We analyze how practical issues such as velocity variations, misleading sampling rates, and local-oscillator frequency offsets can degrade the accuracy of the proposed DoA estimator, highlighting trade-offs between aperture length, snapshot budget, and tolerance to measurement noise. Our results indicate that the proposed signal model for dual-antenna passive synthetic aperture is capable of dealing with even moderate misleading measurements and still arriving at useful azimuth and elevation estimates.**

***Keywords*— Passive Synthetic Aperture, Direction-of-Arrival, Low-SWaP Systems**

I. Introduction

High-resolution DoA estimation is a key enabler for applications such as surveillance, navigation, and electronic warfare [1]. However, classical array-based solutions may impose large hardware footprints with multiple frontend channels [2], making them unsuitable for small platforms such as drones or lightweight aircraft. Passive synthetic aperture methods leverage platform motion to emulate a large array using minimal hardware [3]. Such strategies are well-suited for UAVs, where researchers have investigated techniques of SAR for angular estimation [4]. Nevertheless, single-antenna implementations are typically restricted to azimuth-only estimation and are prone to ambiguities over wide Field-of-View (FoV). By introducing a second receive element, spaced by $\lambda/2$, one can enable two-dimensional angle estimation with a marginal increase in size, weight, and power (SWaP). Such compact configurations remain relatively scarce in the literature, especially under realistic Doppler and spherical-wave effects, as well as potential navigation and synchronization errors.

In our earlier work we developed this line of research in two stages. First, we introduced a *single-antenna* passive synthetic-aperture scheme and showed that platform motion alone can provide accurate DoA estimates in azimuth, provided a sufficiently long virtual aperture and a favourable Signal-to-Noise Ratio (SNR) regime [5]. Building on those results, our contribution extended the concept to a *dual-antenna* configuration, demonstrating that a second element spaced by $\lambda/2$ enables joint azimuth–elevation estimation while retaining a low-SWaP footprint, under the assumptions of perfect trajectory knowledge and negligible local-oscillator (LO) misalignment [6]. In practical airborne deployments, however, positional inaccuracies, velocity fluctuations and residual LO frequency offsets are unavoidable and can severely degrade performance if left unmodelled. This paper therefore quantifies the impact of those real-world uncertainties within the dual-antenna passive synthetic-aperture framework.

Leandro Geraldo da Costa, Rafael S. S. Cruz, Daniele Oliveira Silva, Romildo Henrique de Souza, and Felix Antreich, Department of Telecommunications, Aeronautics Institute of Technology (ITA), São José dos Campos - São Paulo, e-mail: leandrocosta2008@gmail.com, rafaelcruz@ita.br. daniele19954@gmail.com, romildohsouza@gmail.com, and fean@ita.br; This work was partially supported by the Brazilian National Council for Scientific and Technological Development (CNPq) under grant 312394/2021-7 PQ-2, 406517/2022-3, 407245/2022-7, and 313901/2025-2, and by Brazil´s Funding Authority for Studies and Projects (FINEP) under grant 01.22.0581.00.

II. Sensing Scenario

To evaluate the proposed dual-antenna synthetic-aperture system, we consider a representative airborne sensing scenario generated with the *Advanced Radar Simulator (ARS)*. The receiver is equipped with *two* antennas, spaced by $\lambda/2$, arranged in a vertical Uniform Linear Array (ULA), remain oriented toward the radio source. The platform flies eastwards at a constant speed of $v = 200$ m/s and generates a wide virtual aperture in the azimuth direction and provides an instantaneous interferometric baseline in elevation. The emitter is localized by performing DoA estimation at successive positions along the same flight heading. We consider a 200 km Line-of-Sight (LoS) link at near-zero elevation. A summary of the key geometry, platform, and waveform parameters is given in Table I and the virtual arrays and snapshot combinations used in this work with the synthetic aperture (in millimeters) for each pair (K, Q) are shown in Table II.

TABLE I: Scenario parameters.

Geometry & Operating		**Transmit & Signal**	
Par.	**Val.**	**Par.**	**Val.**
LoS [km]	200	f_c [GHz]	26
Sens. alt. [m]	0	PW [ns]	10 000
El. [°]	0	PRP [kHz]	10
Vel. [m/s]	200	Antenna pattern	Omni
Fs [MHz]	200	Doppler	Yes
Ant. pat.	Omni	Freq. off. mod.	No
$\lvert f_d \rvert_{\max}$ [kHz]	~ 17.35	Prop. mod.	Spherical
Radar alt. [m]	0	Sig. type	Rect. pulse

TABLE II: Synthetic-aperture length for (Q, K) pairs.

Q	2	10	20	50	100	500	500	1000
K	1000	200	100	40	20	4	2	2
Synthetic aperture (mm)	0.001	0.009	0.019	0.049	0.099	0.499	0.499	0.999

III. Signal Model

Under the far-field assumption, the signal is assumed to reach the center of the ULA (at position $\mathbf{p}_n$) in discrete time intervals of $(n-1)T_s$, where T_s is the sampling duration and $n = 1, 2, 3, \ldots$. We consider a synthetic aperture along the x-axis with a size of Q consecutive samples. The unit vector

$$\mathbf{u}^{\mathsf{T}} = \left[\, \sin(\theta)\cos(\varphi) \;\; \sin(\theta)\sin(\varphi) \;\; \cos(\theta) \,\right] = \left[\, u_x \;\; u_y \;\; u_z \,\right], \quad (1)$$

oriented perpendicular to the incident planar wavefront, indicates the DoA relative to the antenna coordinate system's center, which moves with the platform for each snapshot $k = 1, \ldots, K$, as shown in Fig. 1. In this synthetic aperture setup with two physical antenna elements, the azimuth angle φ, which is part of the DoA, is measured from the x-axis toward the y-axis, intersecting the projection of $\mathbf{u}$ onto the xy-plane. The elevation angle θ is measured from the z-axis toward $\mathbf{u}$.

We assume the two antennas are separated by a distance $\delta = \lambda/2$, placing them at fixed z-coordinates of $z = \pm\delta/2$. While these antennas are fixed in the vertical dimension, the array (or platform) traverses discrete sampling points along the x-axis with an inter-sampling distance of $\Delta = v_x T_s$, where v_x is the velocity of the platform. The antenna positions in each of the K consecutive blocks, each with its own coordinate system, are denoted by a single expression:

$$\mathbf{d}_{i,k,l} = \left[\left(\tfrac{Q+1}{2} - l\right)\Delta \quad 0 \quad \tfrac{\delta}{2}(-1)^{i+1}\right]^{\mathsf{T}}, \quad i \in \{1, 2\}. \quad (2)$$

Here, the index l denotes the local sample number within a specific block k, where l ranges from 1 to Q. This local index is derived from the absolute sample index n using the relation $l = n - Q(k-1)$. The index i, in turn, distinguishes between the two antennas. This format concisely represents the common x-coordinate and the opposing z-coordinates for each antenna pair.

Thus, the time delay at sensor $\mathbf{d}_{i,k,l} = [d_{i,k,l,x} \;\; d_{i,k,l,y} \;\; d_{i,k,l,z}]^{\mathsf{T}}$ is given by

$$\tau_{i,k,l} = \frac{1}{c}\,\mathbf{u}^{\mathsf{T}}\mathbf{d}_{i,k,l} = \frac{1}{c}\left(\left(\frac{Q+1}{2} - l\right)\Delta\,\sin(\theta)\cos(\varphi) + \frac{\delta}{2}(-1)^{i+1}\,\cos(\theta)\right), \quad (3)$$

where c is the speed of light.

Let $s(t) \in \mathbb{C}$ be a signal impinging on the ULA from $\mathbf{u}$.

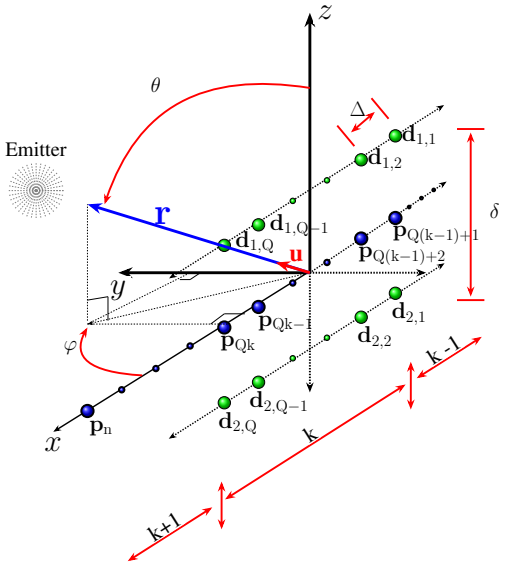

Fig. 1: Synthetic aperture for Q samples and K snapshots.

The complex baseband signal at $\mathbf{d}_{i,k,l}$ is

$$\underbrace{\begin{bmatrix} y_{1,k}((l-1)T_s) \\ y_{2,k}((l-1)T_s) \end{bmatrix}}_{=\mathbf{x}_k[l]} = \begin{bmatrix} s_k\big((l-1)T_s - \tau_{1,k,l}\big)\, e^{-j2\pi f_c \tau_{1,k,l}} \\ s_k\big((l-1)T_s - \tau_{2,k,l}\big)\, e^{-j2\pi f_c \tau_{2,k,l}} \end{bmatrix} + \underbrace{\begin{bmatrix} \mathrm{n}_{1,k}((l-1)T_s) \\ \mathrm{n}_{2,k}((l-1)T_s) \end{bmatrix}}_{=\mathbf{n}_k[l]} \quad (4)$$

where $\mathbf{n}_k[l]$ is additive complex white Gaussian noise with $\mathcal{CN}(0, \sigma_n^2)$. Assuming the signal $s(t)$ is narrowband, for Q consecutive time instances, the difference between consecutive delays can be approximated as

$$\begin{aligned} \tau_{i,k,(l+2)} - \tau_{i,k,(l+1)} \approx \tau_{i,k,(l+3)} - \tau_{i,k,(l+2)} \approx \cdots \\ \approx \tau_{i,k,Q} - \tau_{i,k,Q-1}. \end{aligned} \quad (5)$$

Furthermore, we assume that for Q consecutive samples, also the complex envelope $s_k((l-1)T_s) = s_k[l]$, for $l = 1, 2, \ldots, Q$ can be approximated as

$$s_k[1] \approx s_k[2] \approx s_k[3] \approx \cdots \approx s_k[Q]. \quad (6)$$

Thus, we can write

$$\mathbf{x}_k[l] \approx s_k[l] \begin{bmatrix} e^{-j2\pi f_c \tau_{1,k,l}} \\ e^{-j2\pi f_c \tau_{2,k,l}} \end{bmatrix} + \mathbf{n}_k[l]. \quad (7)$$

Finally, we can rearrange the phase term of the received signal as a left centro-hermitian steering vector $\mathbf{a}(\varphi, \theta, f_c, v_x, T_s)$ for each snapshot k and write the received signal in vector notation. In the expression below, we use $s_k[Q]$, the envelope of the last sample within each block, as the representative

value for the stationary signal envelope.

$$\mathbf{y}[k] \triangleq \underbrace{e^{-j\,\frac{2\pi}{\lambda}\,(k-1)\,Q\,\Delta\,\sin(\theta)\cos(\varphi)} s_k[Q]}_{=\tilde{s}[k]} \underbrace{\begin{bmatrix} e^{+j\,\frac{2\pi\Delta}{\lambda}\left(\frac{Q-1}{2}\,\sin(\theta)\cos(\varphi)+\,\frac{\delta}{2\Delta}\,\cos(\theta)\right)} \\ e^{+j\,\frac{2\pi\Delta}{\lambda}\left(\frac{Q-1}{2}\,\sin(\theta)\cos(\varphi)-\,\frac{\delta}{2\Delta}\,\cos(\theta)\right)} \\ e^{+j\,\frac{2\pi\Delta}{\lambda}\left(\frac{Q-3}{2}\,\sin(\theta)\cos(\varphi)+\,\frac{\delta}{2\Delta}\,\cos(\theta)\right)} \\ e^{+j\,\frac{2\pi\Delta}{\lambda}\left(\frac{Q-3}{2}\,\sin(\theta)\cos(\varphi)-\,\frac{\delta}{2\Delta}\,\cos(\theta)\right)} \\ \vdots \\ e^{-j\,\frac{2\pi\Delta}{\lambda}\left(\frac{Q-3}{2}\,\sin(\theta)\cos(\varphi)-\,\frac{\delta}{2\Delta}\,\cos(\theta)\right)} \\ e^{-j\,\frac{2\pi\Delta}{\lambda}\left(\frac{Q-3}{2}\,\sin(\theta)\cos(\varphi)+\,\frac{\delta}{2\Delta}\,\cos(\theta)\right)} \\ e^{-j\,\frac{2\pi\Delta}{\lambda}\left(\frac{Q-1}{2}\,\sin(\theta)\cos(\varphi)-\,\frac{\delta}{2\Delta}\,\cos(\theta)\right)} \\ e^{-j\,\frac{2\pi\Delta}{\lambda}\left(\frac{Q-1}{2}\,\sin(\theta)\cos(\varphi)+\,\frac{\delta}{2\Delta}\,\cos(\theta)\right)} \end{bmatrix}}_{=\mathbf{a}(\varphi,\theta,f_c,v_x,T_s)} + \underbrace{\begin{bmatrix} \mathbf{n}_k[1] \\ \mathbf{n}_k[2] \\ \vdots \\ \mathbf{n}_k[Q] \end{bmatrix}}_{=\tilde{\mathbf{n}}[k]}$$

$$= \mathbf{a}\big(\varphi,\theta,f_c,v_x,T_s\big)\,\tilde{s}[k] \;+\; \tilde{\mathbf{n}}[k]. \tag{8}$$

Assuming that the angles of arrival φ and θ are constant for K snapshots we can write a signal model in matrix form collecting K snapshots

$$\mathbf{Y} = \mathbf{a}(\varphi,\theta,f_c,v_x,T_s)\,\tilde{\mathbf{s}}^{\mathrm{T}} \;+\; \mathbf{N} \;\in\; \mathbb{C}^{2Q\times K}, \tag{9}$$

where

$$\mathbf{Y} = \big[\,\mathbf{y}[1]\;\mathbf{y}[2]\;\ldots\;\mathbf{y}[K]\,\big], \tag{10}$$

$$\mathbf{N} = \big[\,\tilde{\mathbf{n}}[1]\;\tilde{\mathbf{n}}[2]\;\ldots\;\tilde{\mathbf{n}}[K]\,\big], \tag{11}$$

$$\tilde{\mathbf{s}} = \big[\tilde{s}[1],\tilde{s}[2],\ldots,\tilde{s}[K]\big]^{\mathrm{T}}. \tag{12}$$

Multiplying $s_k[Q]$ by $e^{-j\,\frac{2\pi}{\lambda}\,(k-1)\,Q\,\Delta\,\sin(\theta)\cos(\varphi)}$ implements a global phase shift applied to each snapshot k that compensates for the platform displacement. Hence, the center of the synthetic aperture coordinate system for each snapshot k always coincides with the center of the first snapshot ($k = 1$).

IV. DoA Estimation

In this work, we apply the Maximum Likelihood Estimator (MLE) to estimate the DoA, which for a single impinging wavefront is equivalent to the so-called conventional beamformer applied to DoA estimation [7]. The spatial covariance matrix $\mathbf{R}_{\mathbf{yy}}$ can be estimated from the $2Q \times K$ data matrix $\mathbf{Y}$ as

$$\hat{\mathbf{R}}_{\mathbf{yy}} = \frac{1}{K}\mathbf{Y}\mathbf{Y}^{\mathrm{H}} \in \mathbb{C}^{2Q\times 2Q}. \tag{13}$$

The MLE for the DoA, azimuth and elevation angles, in the single-source case can be given as the solution to the following optimization problem:

$$(\hat{\varphi},\hat{\theta}) = \underset{\varphi,\theta}{\arg\max}\big\{\mathbf{a}^{\mathrm{H}}(\varphi,\theta,f_c,v_x,T_s)\,\hat{\mathbf{R}}_{\mathbf{yy}}\,\mathbf{a}(\varphi,\theta,f_c,v_x,T_s)\big\}. \tag{14}$$

To solve for $(\hat{\varphi},\hat{\theta})$, a two-dimensional grid search is used to roughly estimate the maximum of the likelihood function, and the Nelder-Mead optimization method [8] is applied for refinement.

First, an initial coarse grid search is performed for φ ranging from 0° to 180° and for θ ranging from 90° to 120°, using a resolution of 1° in both cases. These initial coarse searches provide estimates of angles, which are subsequently refined using the Nelder–Mead method, with a tolerance of 10^{-2} for angle parameters and 10^{-14} for the cost function, restricted to a maximum iteration limit of 500. In addition to that, a penalty function terminates the optimization if the angle variation exceeds 5°.

V. Modeling Errors

Real-world systems are subject to imperfections that are not present in the ideal signal model. We analyze the impact of three primary sources of error: navigation inaccuracies, sampling rate deviations, and frequency offsets.

A. Navigation errors

Real airborne trajectories differ from the ideal platform motion due to inertial navigation drift, Global Navigation Satellite Systems (GNSS) measurement inaccuracies, or unexpected velocity changes:

- **Velocity Errors:** A mismatch between the assumed velocity and the true velocity v_x alters the inter-sampling distance $\Delta = v_x T_s$, which is a critical parameter in the steering vector. This introduces a cumulative phase error across the synthetic aperture.

We modeled this as a deterministic bias, where an incorrect velocity is used in the steering vector of the estimator, while the simulated data is generated with the true velocity.

B. Sample rate Mismatch

A mismatch in the sampling rate, T_s, directly affects the calculation of the inter-sampling distance Δ, similar to a velocity error. If the estimator assumes a sampling period T_s' while the true period is T_s, the assumed position of each virtual element will be incorrect, leading to phase errors in the steering vector. This is modeled as a deterministic bias, analogous to the velocity error.

C. Frequency Offsets

In addition to navigation imperfections, local-oscillator (LO) instability introduces a frequency offset, f_{off}. This offset originates from the stability limitations of the system's master reference oscillator, which is typically specified in parts-per-million (ppm). The absolute frequency offset at a given carrier frequency, f_c, can be related to the oscillator's stability, S_{ppm}, as:

$$f_{\text{off}} = S_{\text{ppm}} \times 10^{-6} \times f_c. \tag{15}$$

The phase of the received signal is then impacted by this offset, which modifies the steering vector via the phase term:

$$\phi_n \;\approx\; 2\pi\left(f_c + f_{\text{off}}\right)\tau_n, \tag{16}$$

where τ_n is the nominal delay. Even small offsets can accumulate over the synthetic aperture, degrading the accuracy of the DoA estimates if not accounted for.

VI. Simulations and Analysis

This section presents the results of Monte Carlo simulations, based on 10,000 independent runs, to evaluate the performance of the dual-antenna synthetic-aperture DoA estimator. The simulations adhere to the scenario parameters outlined in Table I. In our *global* coordinate system, the azimuth angle, φ, is measured from the x-axis (0°–180°), and the elevation angle, θ, is measured from the z-axis (0°–180°). To facilitate analysis relative to the array's orientation, we re-center both angles around the virtual antenna boresight:

$$\varphi_{\text{ant}} = \varphi - 90^\circ, \quad \theta_{\text{ant}} = 90^\circ - \theta. \tag{17}$$

A. Error-Free Measurements

We first analyze the estimator's performance assuming ideal measurements, with results evaluated at an SNR of 0 dB. Figure 2 presents the Root-Mean-Square (RMS) azimuth error for various combinations of virtual array size (Q) and snapshot count (K). Several key observations emerge:

- **Azimuth-Dependent Performance:** For short synthetic apertures, the MLE frequently fails to converge to the true angle, often producing estimates at the boundary of the FoV. To prevent such outliers from skewing the results, our algorithm constrains the estimate to $\varphi_{\text{ant}} = 0^\circ$ in these non-convergent cases. This constraint is responsible for the "ramp" effect seen in the RMS error, as estimates across the azimuth range are consistently pulled toward an incorrect angle.
- **Sample-Budget Trade-Off:** For a fixed total sample budget of 2000 ($Q \times K$), increasing the virtual-array size Q yields greater performance gains than increasing the number of snapshots K. This highlights the importance of a longer aperture for robust estimation.
- **Virtual Aperture Size:** As Q increases, estimation accuracy remarkably improves within the $\pm 60^\circ$ boresight region compared to angles at the periphery. The error profile transitions from the non-convergent ramp seen at low Q values to a flat "plateau," a behavior that becomes distinct for $Q \geq 100$.

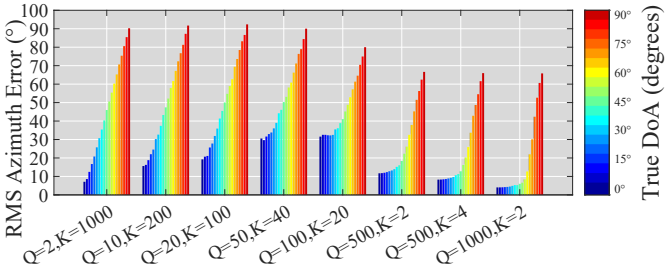

Fig. 2: RMS azimuth error for different synthetic aperture sizes as given in Table II.

In contrast, the RMS error for the elevation estimate, $\hat{\theta}_{\text{ant}}$, is shown in Fig. 3. The results demonstrate stable performance across all (Q, K) configurations, with no significant convergence issues observed across the entire FoV.

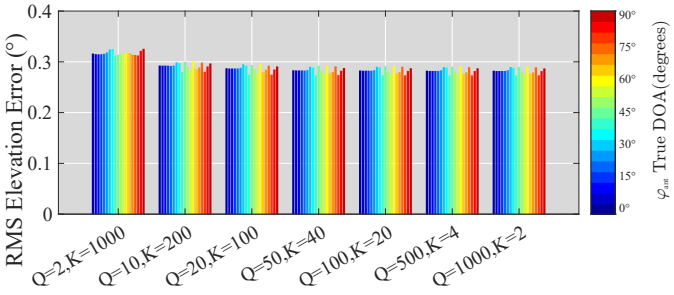

Fig. 3: RMS elevation error at SNR $= 0\,\text{dB}$.

Figure 4 further illustrates the azimuth DoA estimation performance at different angles across a range of SNR values. The synthetic aperture performs best near its boresight ($\varphi_{\text{ant}} \approx 0^\circ$), with estimation error increasing as the true DoA approaches the edges of the FoV. For azimuth angles within $\pm 60^\circ$ of boresight, the system achieves an RMS error below 10 degrees for any SNR greater than 10 dB.

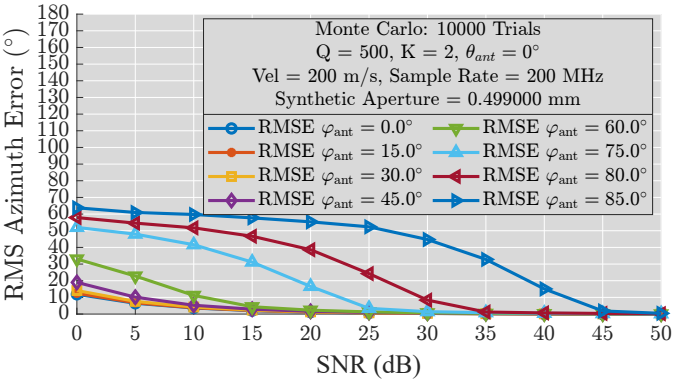

Fig. 4: RMS azimuth error as a function of φ_{ant}.

This angle-dependent performance stems from the intrinsic nature of interferometric phase sensing. The estimator relies on the unwrapped phase difference across the array to infer the Angle-of-Arrival (AoA). The total phase accumulated by a virtual array of Q elements, each spaced by $\Delta = v_x T_s$, is given by:

$$\Phi(\varphi_{\text{ant}}) = 2\pi \, \frac{(Q-1)\,\Delta}{\lambda} \, \cos(\theta_{\text{ant}}) \, \sin(\varphi_{\text{ant}}), \tag{18}$$

where λ is the carrier wavelength. The sensitivity of the phase to a change in the azimuth angle is its derivative:

$$\frac{\mathrm{d}\Phi}{\mathrm{d}\varphi_{\text{ant}}} = 2\pi \, \frac{(Q-1)\,\Delta}{\lambda} \, \cos(\theta_{\text{ant}}) \, \cos(\varphi_{\text{ant}}). \tag{19}$$

Figure 5 plots the total phase from (18) and its sensitivity from (19). Near boresight ($\varphi_{\text{ant}} \approx 0^\circ$), the derivative is maximal, meaning a small change in angle produces a large change in phase, which enables reliable estimation. As the angle moves toward the edges of the FoV ($\pm 90^\circ$), the derivative approaches zero. Beyond approximately $\pm 60^\circ$, the sensitivity drops to half its peak value, causing identical angular variations to produce smaller phase changes and thus inherently degrading DoA accuracy.

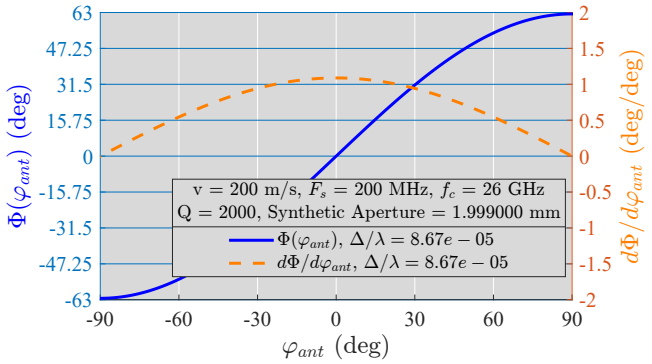

Fig. 5: Total unwrapped phase and its sensitivity.

B. Measurements with Parameter Mismatches

We now assess the estimator's robustness to parameter mismatches between the simulation model and the estimator's assumptions.

Figure 6 shows the impact of a velocity mismatch on the RMS azimuth error. The simulation assumes a true platform velocity of 200 m/s, while the plot presents four curves corresponding to velocities assumed by the estimator: 200 m/s (no error), 150 m/s, 100 m/s, and 50 m/s. It is important to note that the larger deviations are deliberately extreme conditions designed to stress the signal model to its limits. In a practical application, the velocity error from a modern navigation system using GNSS Doppler measurements is expected to be well under 0.1%, with typical accuracies on the order of 0.03 m/s [9]. This makes the simulated test conditions far more severe than those encountered in reality.

Remarkably, the results show that for moderate to high SNR (above 20 dB), the RMS error remains below 5 degrees even with the largest velocity mismatch, demonstrating the model's considerable resilience.

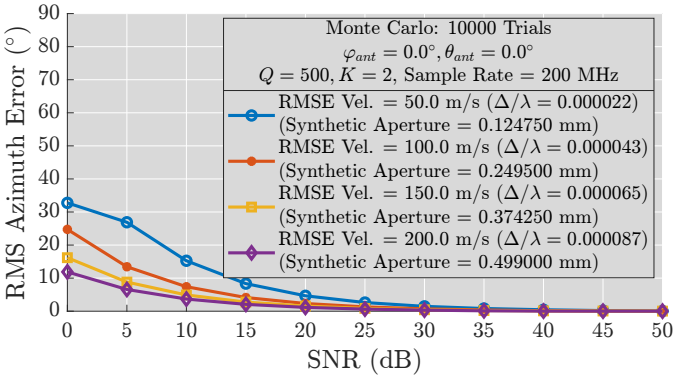

Fig. 6: Impact of velocity mismatch on RMS azimuth error.

Figure 7, in turn, illustrates the performance degradation from a mismatched sampling rate. The plot evaluates the system's performance when the true sampling rate is 200 MHz, while the estimator operates under the mismatched assumptions of 150 MHz and 100 MHz, in addition to the error-free case.

This error originates from the stability limitations of the reference clock in the receivers. For the 26 GHz band, a system would typically employ a mmWave front-end to downconvert the signal before digitization by a high-performance receiver, such as those in the National Instruments mmWave platform [10]. The stability of the reference oscillators in such systems is typically on the order of a few parts-per-million (ppm) [11].

Therefore, the simulated mismatches of 25% (150 MHz) and 50% (100 MHz) are significant overestimations of real-world error, chosen to rigorously test the model's resilience. The system proves to be less sensitive to this type of error compared to velocity errors, with the RMS azimuth error remaining below 10 degrees across the entire simulated SNR range.

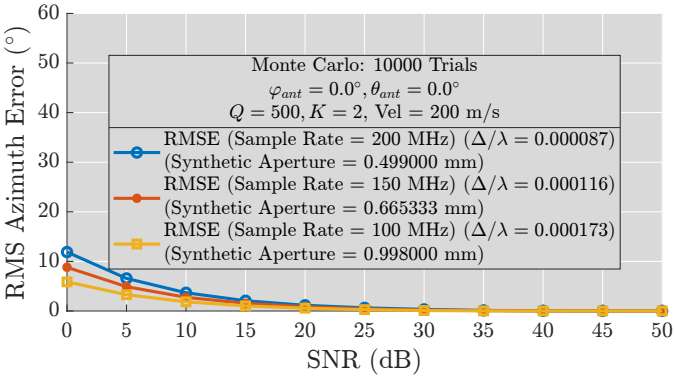

Fig. 7: Impact of sampling rate mismatch.

Figure 8 shows the effect of a static frequency offset on estimation performance. To characterize the estimator's sensitivity in a high-performance setting, this analysis simulates a range of small offsets from 0 Hz to 5 kHz in 1 kHz increments. Based on the model from Section V-C, all of these offsets correspond to a very high oscillator stability (less than 0.2 ppm at 26 GHz), which is achievable with high-grade hardware platforms [10], [11]. The goal is to observe how gracefully the system's performance degrades with small, increasing-but-realistic errors.

The results reveal a clear trend for moderate to high SNR. A regular, nearly linear degradation in RMS azimuth error is observed as the frequency offset increases from 0 to 5 kHz. In this regime, where the system is not limited by noise, its performance is directly impacted by the deterministic bias from the offset. Although the system's short integration time prevents catastrophic failure, the cumulative phase error grows proportionally with f_{off}, leading to this predictable increase in estimation error.

To put this degradation into perspective, at the maximum simulated offset of 5 kHz, the RMS error is approximately 8 degrees for SNR values above 20 dB and exceeds 14 degrees at an SNR of 0 dB. In stark contrast, the baseline case with no frequency offset maintains an RMS error close to zero in the high-SNR regime. This significant impact highlights the necessity of compensating for any known frequency offsets within the signal model. Failing to do so can cause the estimation error to grow rapidly, potentially rendering the DoA estimates unusable for practical applications.

At low SNR (below 20 dB), a different behavior is observed. The performance curves for all simulated offsets are clustered closely together. While a slight increase in error is still

visible as the offset grows, the separation between the curves is significantly reduced. This occurs because, in this noise-limited regime, the estimator's performance is dominated by the high variance of the noise. The small, deterministic error introduced by the frequency offset is largely obscured by this much larger random error component. As the SNR improves, the effect of the offset becomes progressively more apparent.

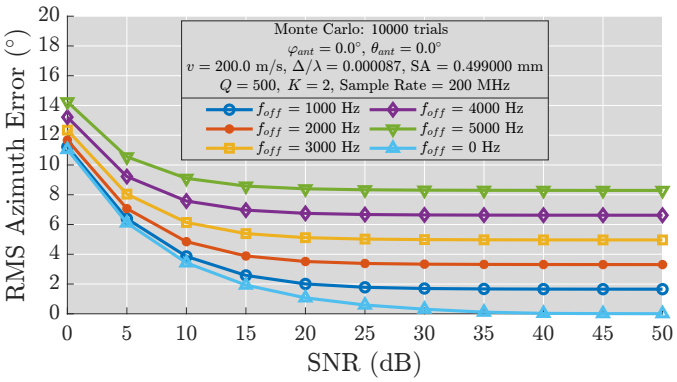

Fig. 8: Impact of frequency offset.

Finally, Figure 9 evaluates the estimator's performance in a realistic scenario where multiple errors are present simultaneously. This test combines a 1% velocity mismatch, a 1% sampling rate mismatch, and a 1000 Hz frequency offset. These plausible error levels are less severe than the maximum values tested in isolation, providing insight into the system's operational robustness.

As seen in the individual analyses (Fig.6 and Fig.7), the chosen mismatches can have competing influences. A velocity underestimation tends to increase RMS error, while the 1% sampling rate mismatch was observed to have a counteracting effect. The 1000 Hz frequency offset, in contrast, consistently contributes to degradation. In this combined scenario, these effects are superimposed, with the frequency offset being the primary contributor to deterministic bias.

Despite these combined errors, the estimator remains effective. The RMS azimuth error stays below 2° for SNR values above 20dB, where the bias becomes most apparent. At lower SNR, particularly near 0dB, the performance curve converges with the error-free case as random noise dominates and obscures deterministic effects. Overall, this validates the model's resilience under plausible, combined real-world imperfections.

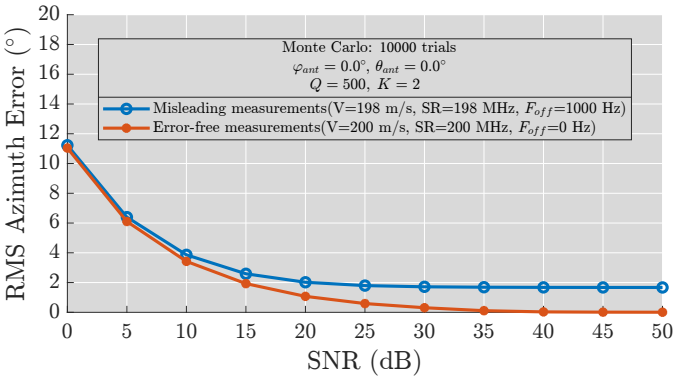

Fig. 9: Impact of combined parameter mismatches.

VII. Conclusion

In this paper, we presented a comprehensive performance analysis of a dual-antenna passive synthetic aperture DoA estimator under simulated real-world uncertainties. By modeling errors in platform velocity, sampling rate, and local oscillator frequency, we evaluated robustness and identified operational limits through extensive Monte Carlo simulations.

Our findings confirm that the proposed low-SWaP system provides accurate joint azimuth and elevation estimates, with performance intrinsically linked to synthetic aperture length and angle relative to boresight. Crucially, our robustness analysis revealed two distinct behaviors. The estimator showed remarkable resilience to extreme mismatches in velocity and sampling rate, with simulated errors far exceeding those expected in practice. Conversely, sensitivity analysis for frequency offset revealed predictable, regular degradation even for small offsets. This highlights that while the system is broadly robust, precise frequency synchronization or compensation is essential for highest accuracy.

We also investigated the scenario where these errors occur concurrently, noting their potential to produce competing effects. Even with this combination of uncertainties, the estimator remained effective, validating its potential for practical airborne applications. This work confirms that dual-antenna passive synthetic aperture is a viable, resilient technique for low-SWaP platforms, offering a clear path toward robust passive sensing in realistic operational environments.

References

[1] S. CHANDRAN, *Advances in Direction-of-Arrival Estimation*. Norwood, MA: Artech House, 2005.

[2] H. L. VAN TREES, *Optimum Array Processing. Detection, Estimation and Modulation Theory, Part IV*. New York, NY: Wiley Interscience, 2002.

[3] J. CHENG, K. GUAN, and F. QUITIN, "Direction-of-arrival estimation with virtual antenna array: Observability analysis, local oscillator frequency offset compensation, and experimental results," *IEEE Transactions on Instrumentation and Measurement*, vol. 70, pp. 1–13, 2021.

[4] I. LLAMAS-GARRO, K. LUKIN, M. T. DE MELO, and J.-M. KIM, "Frequency and angular estimations of detected microwave source using unmanned aerial vehicles," in *2016 IEEE MTT-S Latin America Microwave Conference (LAMC)*, 2016, pp. 1–3.

[5] L. G. d. COSTA, D. O. SILVA, and F. D. ANTREICH, "Single antenna passive synthetic aperture doa estimation," in *Proceedings of the Symposium on Operational Applications in Defense Areas*. São José dos Campos, BR: Instituto Tecnológico de Aeronáutica, 2024.

[6] L. G. d. COSTA, D. O. SILVA, R. H. DE SOUZA, and F. D. ANTREICH, "Dual-antenna passive synthetic aperture doa estimation for airborne platforms," in *Proceedings of the Simpósio Brasileiro de Telecomunicações e Processamento de Sinais (SBrT)*. Rio de Janeiro, BR: Sociedade Brasileira de Telecomunicações, 2025.

[7] N. O'DONOUGHUE, *Emitter Detection and Geolocation for Electronic Warfare*, ser. Artech House electronic warfare library. Boston, MA: Artech House, 2019.

[8] J. A. NELDER and R. MEAD, "A simplex method for function minimization," *The Computer Journal*, vol. 7, no. 4, pp. 308–313, 1965.

[9] M. A. RABBOU and A. EL-RABBANY, "Velocity determination using single point positioning with a low-cost gps receiver," *Journal of Surveying Engineering*, vol. 141, no. 4, p. 04014027, 2015.

[10] NATIONAL INSTRUMENTS, "Introduction to the ni mmwave transceiver system for 5g prototyping," Jul. 2016, white Paper. Available at: https://spectrum.ieee.org/introduction-to-the-ni-mmwave-transceiver-system-hardware.

[11] J. R. VIG, "Quartz crystal resonators and oscillators for frequency control and timing applications – a tutorial," US Army Communications-Electronics Command, Fort Monmouth, NJ, Tech. Rep. ARL-TR-2165, Mar. 2001.